

Effect of crystallinity on spin-orbit torque in 5d iridium oxide IrO₂

Tetsuro Morimoto¹, Kohei Ueda^{1,2,3,a)}, Junichi Shiogai^{1,3}, Takanori Kida⁴,

Masayuki Hagiwara⁴, and Jobu Matsuno^{1,2,3}

¹*Department of Physics, Graduate School of Science, Osaka University, Osaka 560-0043, Japan*

²*Center for Spintronics Research Network, Graduate School of Engineering Science, Osaka University, Osaka 560-8531, Japan*

³*Spintronics Research Network Division, Institute for Open and Transdisciplinary Research Initiatives, Osaka University, Osaka, 565-0871, Japan*

⁴*Center for Advanced High Magnetic Field Science, Graduate School of Science, Osaka University, Osaka 560-0043, Japan*

^{a)}Author to whom correspondence should be addressed: kueda@phys.sci.osaka-u.ac.jp

ABSTRACT

The 5d transition-metal oxides provide an intriguing platform for generating an efficient spin current due to a unique electronic structure dominated by 5d electrons with strong spin-orbit coupling. Here, we report on the effect of crystallinity on current-driven spin-orbit torque (SOT) in binary 5d iridium oxide IrO₂ thin films by controlling amorphous, polycrystalline, and epitaxial states. By conducting harmonic Hall measurement in bilayers composed of ferromagnetic Co₂₀Fe₆₀B₂₀ and IrO₂, we find that dampinglike (DL) SOT is larger than fieldlike SOT for all the samples. We also demonstrate that both electrical resistivity and the DL SOT efficiency increase in order of epitaxial, polycrystalline, and amorphous IrO₂. Despite their different electrical conductivities, spin Hall conductivities of the three states of the IrO₂ layer are found to be nearly constant, which is consistent with the intrinsic regime of the spin Hall effect scaling relation. Our results highlight the important role that crystallinity plays in the spin-current generation, leading to the potential technological development of spintronic devices based on the 5d transition-metal oxides. (169 words)

Spin-orbit coupling (SOC) is a relativistic effect that couples the orbital angular momentum of an electron with its spin angular momentum. Interfaces in bilayers composed of ferromagnet (FM) and non-magnet (NM) with a strong SOC provide a rich playground for exploring emergent spin related phenomena and the underlying physics [1]. One of the most highlighted topics in the FM/NM bilayer is a current-driven spin-orbit torque (SOT) [2,3,4], which is realization of charge to spin current conversion: the SOT is generated by the bulk spin Hall effect (SHE) [5] and/or interface Rashba-Edelstein effect (REE) [6], while both effects are triggered by the strong SOC. Of particular interest is the SOT via the SHE, which demonstrates magnetization switching of the adjacent FM [2,7,8]. For the last decade, the SHE-induced SOT has been further manifested to give rise to highly-efficient motion of chiral spin textures such as magnetic Néel domain walls [9–13] and skyrmions [14,15]. Many previous spintronic studies so far have mainly used *5d* transition metals (TMs) with the strong SOC as NM, such as Pt [2,9,10,12,13,16–18], Ta [7,9,11,14,19–23], and W [8,24,25].

5d transition-metal oxides (TMOs) have recently emerged as a promising class of spintronic materials because of their unique electronic structure; the Fermi surface is dominated only by *5d* electrons with strong SOC, in contrast to that of *5d* TMs dominated by both *5d* and *6s* electrons. Efficient charge to spin-current conversion has been proven by a sizable SOT generation via the SHE in conductive *5d* TMOs such as Ir and W oxides: epitaxial SrIrO₃ [26–30], epitaxial IrO₂ [31,32], amorphous IrO₂ [33,34], and epitaxial WO₂ [35]. One of the advantages of *5d* TMOs is that their epitaxial form can be fully utilized, unlike most of the spintronics studies with *5d* TMs which are primarily focused on polycrystalline films. For instance, the SOT can be controlled in epitaxial Ir oxides by engineering the crystal orientation with the appropriate choice of substrates [28,31,32]. This contrast between epitaxial and polycrystalline forms raises an unsolved question how the crystallinity influences the SOT. Considering that the crystallinity is strongly linked to charge transport properties, e.g., electrical resistivity, the role of the crystallinity in the spin-transport properties is an intriguing subject. Engineering the crystallinity using the *5d* TMOs is therefore an effective approach to further understanding of the spin-current physics via the SOT generation. Among the *5d* TMOs, the particularly promising is the binary IrO₂, which can be a platform to realize the bilayer devices with different crystalline states such as amorphous, polycrystalline, and epitaxial forms. The epitaxial form, namely, rutile IrO₂ structure with a magnetic rutile oxide such as CrO₂, allows creation of a high-quality all oxide epitaxial interface, which is an excellent platform for clarifying intriguing spin-current physics; the CrO₂ is a room-temperature half metal [36,37].

In this paper, we report on the effect of the crystallinity on the SOT by fabricating the three states of the IrO₂. The SOT with dampinglike (DL) and fieldlike (FL) symmetries in Co₂₀Fe₆₀B₂₀ (CoFeB)/IrO₂ bilayers is characterized by harmonic Hall measurement. The DL SOT efficiency

is enhanced with increase of the electrical resistivity, demonstrating that the spin-current properties are strongly affected by their crystallinity. Furthermore, the spin Hall conductivities of the three crystalline states of IrO₂ exhibit nearly constant values despite their different electrical conductivities, consistent with the intrinsic regime of the SHE scaling relation.

We fabricate the IrO₂ thin films by the reactive magnetron sputtering of an Ir target at a working pressure of 0.4 Pa with Ar and oxygen; the sputtering parameters are 75 W for the power and 20% for the partial oxygen pressure. For simplicity, we denote amorphous IrO₂, polycrystalline IrO₂, and epitaxial IrO₂ as a-IrO₂, poly-IrO₂, and epi-IrO₂. In order to selectively grow the three states, we chose a single-crystalline corundum Al₂O₃ (0001) substrate for epi-IrO₂ and thermally oxidized Si substrates for poly-IrO₂ and a-IrO₂; the thermally oxidized Si is prepared by coating a 500-nm-thick amorphous SiO₂ layer deposited on Si substrate. Fixed substrate temperature is at 350 °C for epi-IrO₂ and poly-IrO₂, and ambient temperature for a-IrO₂, respectively. We prepared the single layer IrO₂ films with its thickness of 30 – 40 nm for structural characterization by *x*-ray diffraction (XRD) and *x*-ray reflectivity (XRR) measurement. Figure 1(a) shows a schematic of crystal structure of rutile IrO₂ [38]. The lattice vector represents the rutile unit cell: $a = b > c$, where $a = b = 0.4498$ nm, and $c = 0.3154$ nm for bulk [38]. We draw a simplified sketch of surface oxygen–oxygen arrangement to aid in understanding the crystallographic relationship between IrO₂ and Al₂O₃ as discussed later. The Al₂O₃ has the hexagonal Bravais lattice with an in-plane lattice constant of 0.476 nm [39]. While the gray area represents the *a*-axis-oriented IrO₂ plane, the green, purple, and yellow areas correspond to its in-plane rotation of 30°, 150°, and 270° on the (0001)-oriented Al₂O₃ plane, respectively.

Figure 1(b) shows the out-of-plane XRD pattern of epi-IrO₂ grown on Al₂O₃(0001) substrate. We observe two peaks, (100) and (200), of the rutile IrO₂ without any impurity peaks. The inset of Fig. 1(b) shows the magnified view around the IrO₂(200) and the Al₂O₃(0006) peaks. The IrO₂(200) peak yields an out-of-plane lattice constant of 0.4623 nm, which is close to the previously reported value of ~0.4604 nm for the epitaxial IrO₂(100) grown on TiO₂(100) substrate [40]. The Laue fringes around the (200) diffraction peak evidence a good crystallinity of the film, which is also supported by the narrow full width at half maximum of the rocking curve around IrO₂(200) (~ 0.030 deg.). In order to understand the in-plane crystallographic orientation of the epi-IrO₂, we measured the azimuthal angle ϕ scan at the IrO₂(101) [top panel in Fig. 1(c)] and Al₂O₃($\bar{1}\bar{2}12$) [bottom panel in Fig. 1(c)] diffractions. The three diffraction peaks of Al₂O₃($\bar{1}\bar{2}12$) and its equivalents reflect the three-fold symmetry of the corundum structure [35,41]. The six-fold diffraction peaks of IrO₂(101) and its equivalent (110) were observed, which were rotated by 30° with respect to Al₂O₃($\bar{1}\bar{2}12$). We therefore ascribe the observed six peaks of IrO₂ (101) and (110) to the formation of three crystalline domains with the epitaxial relationship of rutile IrO₂[001](100)//Al₂O₃[$10\bar{1}0$](001) and the other two equivalent orientations as depicted in

Fig. 1(a). Figure 1(d) shows the out-of-plane XRD patterns of poly-IrO₂ and a-IrO₂ grown on thermally oxidized Si substrates. Several diffraction peaks from IrO₂(110), (200), and (211) were observed for poly-IrO₂, while no significant peak was detected for a-IrO₂, confirming that crystallinity was able to be controlled by growth condition and substrate selection; we also confirmed that the valence states are both Ir⁴⁺ for a- and poly-IrO₂, based on their mass densities obtained from the XRR measurements (see APPENDIX A). Moreover, poly-IrO₂ exhibits a crystallite size of ~ 7 nm, as determined from the full width at half maximum of the IrO₂(200) diffraction peak shown in Fig. 1(d) (see APPENDIX B). In contrast, the presence of Laue fringes in epi-IrO₂ suggests that its crystallite size is comparable to the film thickness (~30 nm). These results support distinct crystallinities between poly-IrO₂ and epi-IrO₂. Given this evidence of crystallinity, we thus demonstrated fabrication of IrO₂ films with three distinct crystalline states for investigating spin current generation. We prepared bilayers consisting of ferromagnetic Co₂₀Fe₆₀B₂₀ (referred as CoFeB hereafter) and IrO₂ to examine the effect of crystallinity of IrO₂ thin films on SOT. The whole film structures are represented by TiO_x(2) capped CoFeB(3)/IrO₂(*t*) bilayer on substrate, where the number in parenthesis indicates the thickness in nanometer [Fig. 2(a)]. We vary the thickness of the IrO₂ layer *t* from 4 to 10 nm to characterize its electrical transport properties. After the IrO₂ growth, Ti and CoFeB were deposited in-situ by a radio frequency magnetron sputtering at an Ar deposition pressure of 0.4 Pa. The TiO_x layer was obtained by natural oxidation of the as-deposited Ti metal in the air; it prevents the CoFeB layer from oxidization. We confirmed no SOT contribution from the TiO_x layer by control experiment. The CoFeB and TiO_x thicknesses were estimated from the growth rate of each layer determined by the XRR measurement for thick reference samples. In comparison with the IrO₂, we also prepared an Ir control sample for proving the validity of our SOT measurement set-up, that is, TiO_x(2)/CoFeB(3)/Ir(6) on the thermally oxidized Si substrate. The CoFeB/IrO₂ and CoFeB/Ir bilayers were patterned into a Hall bar with two arms by photolithography and Ar ion milling. Ti(5)/Pt(60) contact pads were attached at the end of devices for electrical measurement. As shown in Fig. 2(a), channel length (*L*) and width (*w*) of the Hall-bar devices are *L* = 30 μm and *w* = 10 μm for epi-IrO₂, and *L* = 50 μm and *w* = 10 μm for the poly- and a-IrO₂ samples. We define *x* and *y* axis as longitudinal and transverse direction of the Hall bar devices. The ϕ_H represents the azimuthal angles of the external magnetic field (*B*_{ext}) in *xy* plane. In order to examine anisotropic SOT [30, 31, 42] for epi-IrO₂, we patterned two orthogonal Hall bars along in-plane orientations [10 $\bar{1}$ 0] and [1 $\bar{2}$ 10] of the Al₂O₃ substrate, while the anisotropic effect can be averaged out by the multiple crystalline domains demonstrated in Fig. 1(c). We applied an ac current $I_{ac} = \sqrt{2}I_{rms} \sin(2\pi ft)$ with root mean square of current *I*_{rms} and frequency *f* = 13 Hz. We set *I*_{rms} to be 0.1 mA for longitudinal resistance (*R*) measurement and Hall resistance (*R*_H) measurement, and 1.5– 2.0 mA for harmonic Hall measurement.

We first characterized electrical transport properties of the IrO₂ layer by t dependence of sheet conductance $L/(Rw)$ shown in Fig. 2(b); the linear fitting yields electrical conductivity σ of the IrO₂ layer. We obtained the electrical resistivity $\rho (= 1/\sigma)$ of $\rho = 350 \mu\Omega\text{cm}$ for a-IrO₂, $210 \mu\Omega\text{cm}$ for poly-IrO₂, and $140 \mu\Omega\text{cm}$ for epi-IrO₂. The ρ values of epi-IrO₂ along the $[10\bar{1}0]$ and $[1\bar{2}10]$ of the Al₂O₃ substrate are equal, which is consistent with multi-domain nature of IrO₂ on Al₂O₃ as discussed in Fig. 1(c). Assuming the resistivity of CoFeB to be the previously obtained value of $165 \mu\Omega\text{cm}$ [30], we determined $\rho = 25 \mu\Omega\text{cm}$ for Ir metal as control sample, which is comparable to previous reports [33,43]. Figure 2(c) summarizes the ρ of the three states of IrO₂ layer, indicating that the ρ monotonically decreases with the improvement in the crystallinity of IrO₂.

We independently quantify DL SOT and FL SOT by performing harmonic Hall measurements as described in Refs. [16,17,20]. By applying the I_{ac} to the Hall bar, the SOT is induced at the FM/NM interface, which has two components with different symmetries, namely, DL and FL SOTs [3]. These SOTs correspond to DL effective field $B_{DL} \parallel (s \times m)$ and FL effective field $B_{FL} \parallel s$, where m and s represent the directions of the magnetization and accumulated spin polarization at the interface; the s is oriented along the y -axis direction. Of these two SOTs, the DL SOT is only relevant to magnetization switching [2,3,4,7]. In order to distinguish the B_{DL} and B_{FL} , the harmonic Hall measurements were performed by measuring the ϕ_H dependence of the first and second harmonic resistances ($R_H^{1\omega}$, $R_H^{2\omega}$) at B_{ext} varying 0.087–1.191 T. The $R_H^{1\omega}$ corresponds to the conventional dc Hall measurement, while the $R_H^{2\omega}$ reflects the influence of SOT; the former and the latter obey Eqs. (1) and (2) [16,17,20],

$$R_H^{1\omega} = R_{PHE} \sin 2\phi_H \quad (1)$$

$$R_H^{2\omega} = - \left(R_{AHE} \frac{B_{DL}}{B_{ext} + B_k} + R_{\nabla T} \right) \cos \phi_H + 2R_{PHE} \frac{B_{FL} + B_{Oe}}{B_{ext}} (2 \cos^3 \phi_H - \cos \phi_H) \quad (2)$$

$$\equiv -R_{DL+\nabla T} \cos \phi_H + R_{FL+Oe} (2 \cos^3 \phi_H - \cos \phi_H) \quad (3)$$

Here, R_{PHE} , R_{AHE} , B_k , $R_{\nabla T}$, and B_{Oe} correspond to planar Hall resistance, anomalous Hall resistance, out-of-plane anisotropy field, thermal induced second-harmonic resistance, such as the anomalous Nernst effect [44] and spin Seebeck effect [45], and current induced Oersted field, respectively. R_{AHE} and B_k were estimated by out-of-plane magnetic field dependence of Hall resistance. The ϕ_H dependence of $R_H^{2\omega}$ is induced by the small modulation of the magnetization from its equilibrium position owing to the current-driven SOTs. We can define the DL contribution ($R_{DL+\nabla T}$) and the FL contribution (R_{FL+Oe}) as the coefficients of the $\cos \phi_H$ and $(2 \cos^3 \phi_H - \cos \phi_H)$ in Eq. (3). We now take a look on the experimental data. The upper panel of Fig. 3(a) shows the representative $R_H^{1\omega}$ as a function of ϕ_H in CoFeB(3)/epi-IrO₂(6) measured at

0.087 and 0.992 T, where the overall trend is reproduced by Eq. (1). A slight deviation of $R_H^{1\omega}$ from Eq. (1) is attributed to anomalous Hall effect (AHE) resulting from a small sample misalignment [20,28,30,34]. By confirming that the AHE contribution is within 3% on the $R_H^{1\omega}$, which is negligibly small compared with R_{PHE} , we thus determined the R_{PHE} from fitting based on Eq. (1). The bottom panel of Fig. 3(a) shows the corresponding result of $R_H^{2\omega}$, which is well fitted by Eq. (2). The difference in amplitude of the $R_H^{2\omega}$ depending on the B_{ext} indicates the suppression of SOTs by the B_{ext} . We estimated the $R_{\text{DL}+T}$ and $R_{\text{FL}+\text{Oe}}$ from the $R_H^{2\omega}$ fitting, which is displayed in the top panel and the bottom panel in Fig. 3(b), respectively. The result indicates the contribution of $R_{\text{DL}+T}$ is larger than that of $R_{\text{FL}+\text{Oe}}$ to the $R_H^{2\omega}$ in the CoFeB/epi-IrO₂ bilayer.

We extract two SOT effective fields B_{DL} and B_{FL} by analyzing magnetic field dependence of $R_{\text{DL}+\nabla T}$ and $R_{\text{FL}+\text{Oe}}$. Figure 3(c) shows the $R_{\text{DL}+\nabla T}$ as a function of $1/(B_{\text{ext}} + B_{\text{K}})$ for CoFeB/epi-IrO₂, which obeys the first term in Eqs. (2) and (3). The slope and intercept of the $R_{\text{DL}+\nabla T}$ correspond to the B_{DL} and the $R_{\nabla T}$, respectively. We determined the DL effective field per current density B_{DL}/J , where J is the applied charge current density flowing in the IrO₂ layer. Based on the parallel resistor model as discussed in Fig. 2, we calculate J . The estimated B_{DL}/J is $+0.143 \text{ mT}/(10^{11} \text{ Am}^{-2})$, suggesting the DL SOT generation in epi-IrO₂. The corresponding result of $R_{\text{FL}+\text{Oe}}$ is plotted as a function of $1/B_{\text{ext}}$ as shown in Fig. 3(d). The $R_{\text{FL}+\text{Oe}}$ has linear dependence on $1/B_{\text{ext}}$, which agrees with the second term in Eqs. (2) and (3). The B_{FL}/J is determined to be $-0.126 \text{ mT}/(10^{11} \text{ Am}^{-2})$ by subtracting the B_{Oe} contribution estimated by Ampere's law as $B_{\text{Oe}} = \mu_0 J t / 2$, where μ_0 is the magnetic permeability in a vacuum.

We then evaluate the SOT efficiency $\zeta_{\text{DL}(\text{FL})}$ from $B_{\text{DL}(\text{FL})}/J$ using the following equation [46]:

$$\zeta_{\text{DL}(\text{FL})} = \frac{2eM_s d B_{\text{DL}(\text{FL})}}{\hbar J} \quad (4)$$

where e , M_s , d , and \hbar are the elementary charge, the saturation magnetization, the magnetic layer thickness, and the Dirac constant, respectively. The M_s for all the films was obtained to be $(0.92-1.0) \times 10^6 \text{ A/m}$ by using a superconducting quantum interference device magnetometer, in agreement with typical value of CoFeB thin films [7,8,11,19,24,25,43]. The ζ_{DL} for epi-IrO₂ (100) with $J//\text{Al}_2\text{O}_3$ ($10\bar{1}0$) is determined to be $+0.013$. We performed the same experiment and analysis for the other samples. We estimate the $\zeta_{\text{DL}} = +0.014$ for epi-IrO₂ (100) with $J//\text{Al}_2\text{O}_3$ ($1\bar{2}10$), $+0.053$ for poly-IrO₂, and $+0.089$ for a-IrO₂ as summarized in Fig. 3(e), while Ir metal shows $+0.008$ (not shown). The ζ_{DL} values for all investigated IrO₂ and Ir films has different magnitude

with the positive sign. The ζ_{DL} for a-IrO₂ and Ir metal is in close agreement with the literature values [33,34,43], demonstrating the validity of our experimental set-up. Compared to other 5d oxides, the ζ_{DL} for IrO₂ (0.01–0.09) in the present study is lower than 0.15–0.55 for epitaxial SrIrO₃ [26,27,30] and +0.17 for epitaxial WO₂ [35]. Despite these relatively low ζ_{DL} values, we have demonstrated the impact of the crystallinity of IrO₂ on SOT. The epi-IrO₂ (100) has the almost same magnitude of ζ_{DL} for two current directions, indicating that the in-plane anisotropic SOT is smeared out by multi-domain formation. Judging from the negligible anisotropic effect of SOT and ρ , we hereafter consider the two devices as identical, resulting in the ζ_{DL} for epi-IrO₂ determined as the average value of +0.014. In contrast to the epi-IrO₂, the magnitude of ζ_{DL} for poly-IrO₂ consists of the averaged contributions from various crystal orientations [Fig. 1(d)]. The poly-IrO₂ is found to exhibit a smaller ζ_{DL} compared to the a-IrO₂, giving the ratio of a-IrO₂/poly-IrO₂ \sim 1.68. Previous study has shown the corresponding ratio of \sim 1.63 in the spin Hall angle θ_{SH} , with 0.065 for a-IrO₂ and 0.040 for poly-IrO₂, extracted from the inverse SHE technique based on non-local transport measurement [47]. Given the conventional formula $\zeta_{\text{DL}} = T_{\text{int}}\theta_{\text{SH}}$, the observed coincidence between ζ_{DL} and θ_{SH} reveals that the spin transparency T_{int} at the interface of IrO₂ and CoFeB is nearly the same for a-IrO₂ and poly-IrO₂. Figure 3(f) shows the ζ_{DL} as a function of the ρ for the epi-, poly, and a- IrO₂ layers. The ζ_{DL} and ρ concomitantly increase in order of epi-IrO₂, poly-IrO₂, and a- IrO₂, indicating the significant role of crystallinity on the spin-current and electrical transport properties. We will further discuss the trend between the ζ_{DL} and the ρ later. Regarding the FL SOT, we obtain $\zeta_{\text{FL}} = -0.010$ for the epi-IrO₂ (100), -0.022 for poly-IrO₂, -0.015 for a-IrO₂, and $+0.004$ for Ir metal. The ζ_{FL} in all the IrO₂ samples are negative and their magnitudes are smaller than those of the corresponding ζ_{DL} , which exhibit positive signs; this difference in sign suggests that the origin of FL SOT is distinct from that of the DL SOT. While it is sometimes attributed to interfacial REE in metallic bilayers [16,17,19,20,24], its precise origin remains under active debate in spintronics. The larger ζ_{DL} than ζ_{FL} is helpful for demonstrating the magnetization switching since the DL SOT plays an important role in magnetization control.

We now discuss the SHE scaling relation to gain further insight into how ζ_{DL} correlates with the crystallinity. The SHE scaling relation has been much less experimentally investigated than the AHE mainly because the SHE is achieved only in metals with high conductivity. It is theoretically proposed that the SHE obeys the same scaling relation as the AHE since both the SHE and the AHE originate from the intrinsic and the extrinsic mechanisms arising from the SOC [48,49]. In the widely investigated AHE scaling relation between the anomalous Hall conductivity σ_{AH} and the electrical conductivity $\sigma (= 1/\rho)$, the AHE is classified into three regimes [50]: dirty ($\sigma_{\text{AH}} \propto \sigma^{1.6}$), intermediate (intrinsic, $\sigma_{\text{AH}} = \text{constant}$), and clean (extrinsic, $\sigma_{\text{AH}} \propto \sigma$). Based on the concept, we plot the spin Hall conductivity σ_{SH} as a function of σ for the three crystalline forms

of IrO₂ in Fig. 4, with the AHE scaling relation indicated by black line [50] and with the σ_{SH} for polycrystalline Pt deposited at various growth rate [51]. Here, the σ_{SH} for IrO₂ is defined by $\sigma_{\zeta_{\text{DL}}}$ with the assumption of $T_{\text{int}} = 1$, which is similar to previous reports [15,23,31]. The σ_{SH} for a-IrO₂ and poly-IrO₂ coincides at $2.5 \times 10^2 \Omega^{-1}\text{cm}^{-1}$, whereas that for epi-IrO₂ ($1.0 \times 10^2 \Omega^{-1}\text{cm}^{-1}$) is smaller than them. Since the theoretical scaling relationship neglects anisotropy of materials [50], we have to consider average of anisotropic spin Hall conductivities when comparing our results with the theory; we judged that the poly-IrO₂ takes the average value of σ_{SH} because it consists of several crystal orientations discussed in Fig. 1(d). In contrast, previous studies have demonstrated the growth of epitaxial IrO₂ films on lattice-matched TiO₂ substrates with various crystal orientations, revealing that (001)-oriented IrO₂ exhibits twice larger spin Hall conductivity than (110)-oriented IrO₂ [31,32]. Considering that IrO₂ has a tetragonal rutile structure with *c*-axis as a fourfold rotational screw axis, we expect that σ_{SH} of our (100)-oriented epi-IrO₂ is close to that of (110)-oriented IrO₂ and hence is smaller than that of (001)-oriented IrO₂; hypothetical averaged σ_{SH} for epi-IrO₂ might be larger than the observed value of $1.0 \times 10^2 \Omega^{-1}\text{cm}^{-1}$. In addition to the spin Hall conductivity, the reported crystal-orientation dependence of electrical conductivity in IrO₂ films grown on TiO₂ substrates, ranging from 3.85×10^3 to $1.25 \times 10^4 \Omega^{-1}\text{cm}^{-1}$, indicates a variation by a factor of approximately 3 [40]. This also suggests that the hypothetical averaged conductivity expected for single-crystalline IrO₂ is unlikely to be significantly higher than that of our film. These findings indicate that the anisotropies in both spin Hall conductivity and electrical conductivity are not large enough to cause a substantial deviation in the log-log plot in Fig. 4. Given the discussion, although our epitaxial IrO₂ film is not perfectly single-crystalline in the in-plane direction, our experimental approach remains valid, since performing SOT and conductivity measurements for all possible crystal orientations would not yield substantially more insight beyond what is already discussed. We can therefore conclude that the three data points for IrO₂ are nearly constant, which is consistent with the intrinsic regime. The σ_{SH} for the Pt is almost constant for their wide range of σ , again indicating the intermediate regime. In our results for IrO₂, we can extend the σ down to $3 \times 10^3 \Omega^{-1}\text{cm}^{-1}$, which is close to the boundary between the dirty and intermediate regimes. Our results experimentally reinforce the agreement between the SHE and the AHE scaling relationship, even in the less conductive compounds such as amorphous IrO₂.

In conclusion, we studied the SOT generation in the CFB/IrO₂ bilayers, where the three crystalline states of the IrO₂ layer were prepared by the reactive sputtering method. The structures of the epi-IrO₂ (100), poly-IrO₂, and a-IrO₂ layers were characterized by the XRD. By conducting harmonic Hall measurement, we estimated the ζ_{DL} values of +0.014 for epi-IrO₂, +0.053 for poly-IrO₂, and +0.089 for a-IrO₂, which monotonically increase with their respective ρ values. These results indicate that engineering crystallinity provides an efficient route for controlling the SOT. Moreover, the σ_{SH} remains nearly constant with respect to their σ , highlighting that the intrinsic

regime of the SHE scaling relation is dominant in the spin-current property. This work paves a new pathway for engineering the charge to spin-current conversion efficiency in $5d$ TMOs, leading to the development of low-power spintronic devices.

APPENDIX A: Discussion for valence state of Ir^{4+} in amorphous IrO_2 and polycrystalline IrO_2 films using mass density measurements obtained through XRR

As shown in Fig. 5(a), the wide-range XRR profiles for amorphous and polycrystalline IrO_2 films grown on Si substrates exhibit similar overall reflectivity features, indicating comparable thicknesses and density ranges. To quantitatively extract the film parameters, we fitted the experimental XRR data in Fig. 5(b) using a theoretical model in which a uniform, single-composition IrO_2 film is grown on a SiO_2 substrate with zero surface roughness. The fitting was performed using the GenX software package [52]. Among the fitting parameters such as film surface roughness, film thickness, and mass density, the primary focus was on determining the mass density with high accuracy. The best-fit results yielded a thickness of approximately 35 nm and a surface roughness of 0.5 nm for both films. We obtained the fitted mass densities for ρ_M (a- IrO_2) = 11.0 g/cm³ and ρ_M (poly- IrO_2) = 11.9 g/cm³, indicating that the amorphous film is ~8% less dense than the polycrystalline one. This finding is consistent with theoretical predictions; although the unit-cell volume of a- IrO_2 cannot be easily measured, a prior theoretical report suggests a 9% lower mass density for amorphous IrO_2 (10.7 g/cm³) compared to crystalline IrO_2 (11.7 g/cm³) [53]. The low-angle XRR profiles in Fig. 5(c) further emphasize this difference, with red and blue triangles indicating the critical angles for a- IrO_2 and poly- IrO_2 , respectively. These critical angles were calculated from the fitted mass densities using the following relation:

$$\theta_c = \sqrt{\frac{r_e \lambda^2}{\pi} \cdot \frac{Z}{A} \cdot N_A \cdot \rho_M}$$

where θ_c is the critical angle, r_e is the classical electron radius, λ is the x-ray wavelength, Z is the total number of electrons per formula unit, A is the molar mass of the formula unit, N_A is Avogadro's number, and ρ_M is the mass density. The good agreement between the calculated critical angles and experimental data further supports the reliability of the fitting results. Given the agreement between the fitted densities and theoretical expectations, and assuming the same IrO_2 stoichiometry, we conclude that the oxygen content is equivalent within experimental error. This supports the view that both films predominantly contain valence state of Ir^{4+} .

APPENDIX B: Distinct crystallinities between polycrystalline and epitaxial IrO_2 films

To provide further insight into crystallinity, we estimated a crystallite size of (D) for poly-IrO₂ according to Scherrer equation via $D = 0.9\lambda/(w\cos\theta)$, where λ is the x ray wave length, w is the full width at half maximum of diffraction pattern, and θ is the Bragg's angle [54]. Figure 6 represents the magnified view of x ray diffraction pattern for poly-IrO₂(200) film. By determining $w = 1.23$ from black fitting curve, we estimated $D \sim 7$ nm, which is significantly smaller than total thickness of 30 nm. In contrast, the presence of Laue fringes in epi-IrO₂ in Fig. 1(b) suggests that its crystallite size is comparable to the film thickness (~ 30 nm). These results provide supportive information for distinct crystallinity between poly- and epi-IrO₂ films.

ACKNOWLEDGEMENT

The authors thank T. Arakawa for technical support. This work was partly carried out at the Center for Advanced High Magnetic Field Science in Osaka University under the Visiting Researcher's Program of the Institute for Solid State Physics, the University of Tokyo. This work was partly supported by Nanotechnology Platform of MEXT, Grant Number JPMXP09S21OS0027, the JSPS KAKENHI (Grant Nos. JP19K15434, JP19H05823, 22H04478, and 24H01666), JPMJCR1901 (JST-CREST), the MEXT "Spintronics Research Network of Japan (Spin-RNJ)", Nippon Sheet Glass foundation for Materials Science and Engineering, and Iketani Science and Technology Foundation. We acknowledge stimulating discussions at the meeting of the Cooperative Research Project of the Research Institute of Electrical Communication, Tohoku University.

ORCID iDs

Kohei Ueda <https://orcid.org/0000-0003-4967-2249>

Junichi Shiogai <https://orcid.org/0000-0002-5464-9839>

Takanori Kida <https://orcid.org/0000-0003-3650-3534>

Masayuki Hagiwara <https://orcid.org/0000-0002-1087-521X>

Jobu Matsuno <https://orcid.org/0000-0002-3018-8548>

REFERENCES

- 1) Y. Otani, M. Shiraishi, A. Oiwa, E. Saitoh, and S. Murakami, Spin conversion on the nanoscale, *Nat. Phys.* **13**, 829 (2017).
- 2) I. M. Miron, K. Garello, G. Gaudin, P. J. Zermatten, M. V. Costache, S. Auffret, S. Bandiera, B. Rodmacq, A. Schuhl and P. Gambardella, Perpendicular switching of a single ferromagnetic layer induced by in-plane current injection, *Nature* **476**, 189 (2011).
- 3) A. Manchon, I. M. Miron, T. Jungwirth, J. Sinova, J. Železny, A. Thiaville, K. Garello, and P. Gambardella, Current-induced spin-orbit torques in ferromagnetic and antiferromagnetic

- systems, *Rev. Mod. Phys.* **91**, 035004 (2019).
- 4) X. Han, X. Wang, C. Wan, G. Yu, and X. Lv, Spin-orbit torques: Materials, physics, and devices, *Appl. Phys. Lett.* **118**, 120502 (2021).
 - 5) A. Hoffmann, Spin Hall Effects in Metals, *IEEE Trans. Magn.* **49**, 5172 (2013).
 - 6) V. M. Edelstein, Spin polarization of conduction electrons induced by electric current in two-dimensional asymmetric electron systems, *Solid State Commun.* **73**, 233 (1990).
 - 7) L. Liu, C.-F. Pai, Y. Li, H. W. Tseng, D. C. Ralph, and R. A. Buhrman, Spin-Torque Switching with the Giant Spin Hall Effect of Tantalum, *Science* **336**, 555 (2012).
 - 8) C. F. Pai, L. Liu, Y. Li, H. W. Tseng, D. C. Ralph, and R. A. Buhrman, Spin transfer torque devices utilizing the giant spin Hall effect of tungsten, *App. Phys. Lett.* **101**, 122404 (2012).
 - 9) S. Emori, U. Bauer, S. M. Ahn, E. Martinez, and G. S. D. Beach, Current-driven dynamics of chiral ferromagnetic domain walls, *Nat. Mater.* **12**, 611 (2013).
 - 10) K.-S. Ryu, L. Thomas, S.-H. Yang, and S. S. P. Parkin, Chiral spin torque at magnetic domain walls, *Nat. Nanotechnol.* **8**, 527 (2013).
 - 11) J. Torrejon, J. Kim, J. Sinha, S. Mitani, M. Hayashi, M. Yamanouchi, and H. Ohno, Interface control of the magnetic chirality in CoFeB/MgO heterostructures with heavy-metal underlayers, *Nat. Commun.* **5**, 4655 (2014).
 - 12) K. Ueda, K. J. Kim, Y. Yoshimura, R. Hiramatsu, T. Moriyama, D. Chiba, H. Tanigawa, T. Suzuki, E. Kariyada, and T. Ono, Transition in mechanism for current-driven magnetic domain wall dynamics, *Appl. Phys. Express* **7**, 053006 (2014).
 - 13) K. Ueda, K. J. Kim, T. Taniguchi, T. Tono, T. Moriyama, and T. Ono, In-plane field-driven crossover in the spin-torque mechanism acting on magnetic domain walls in Co/Ni, *Phys. Rev. B* **91**, 060405(R) (2015).
 - 14) W. Jiang, P. Upadhyaya, W. Zhang, G. Yu, M. B. Jungfleisch, F. Y. Fradin, J. E. Pearson, Y. Tserkovnyak, K. L. Wang, O. Heinonen, S. G. E. te Velthuis, and A. Hoffmann, Blowing magnetic skyrmion bubbles, *Science* **349**, 283 (2015).
 - 15) S. Woo, K. Litzius, B. Krüger, M.-Y. Im, L. Caretta, K. Richter, M. Mann, A. Krone, R. Reeve, M. Weigand, P. Agrawal, P. Fischer, M. Kläui, and G. S. D. Beach, Observation of room-temperature magnetic skyrmions and their current-driven dynamics in ultrathin metallic ferromagnets, *Nat. Mater.* **15**, 501 (2016).
 - 16) K. Garello, I. M. Miron, C. O. Avci, F. Freimuth, Y. Mokrousov, S. Blügel, S. Auffret, O. Boulle, G. Gaudin and P. Gambardella, Symmetry and magnitude of spin-orbit torques in ferromagnetic heterostructures, *Nat. Nanotechnol.* **8**, 587, (2013).
 - 17) C. F. Pai, Y. X. Ou, L. H. Vilela-Leao, D. C. Ralph, and R. A. Buhrman, Dependence of the efficiency of spin Hall torque on the transparency of Pt/ferromagnetic layer interfaces, *Phys. Rev. B* **92**, 064426 (2015).

- 18) W. Zhang, W. Han, X. Jiang, S.-H. Yang, and S. S. P. Parkin, Role of transparency of platinum–ferromagnet interfaces in determining the intrinsic magnitude of the spin Hall effect, *Nat. Phys.* **11**, 496 (2015).
- 19) J. Kim, J. Sinha, M. Hayashi, M. Yamanouchi, S. Fukami, T. Suzuki, S. Mitani and H. Ohno, Layer thickness dependence of the current-induced effective field vector in Ta|CoFeB|MgO, *Nat. Mater.* **12**, 240 (2013).
- 20) C. O. Avci, K. Garello, M. Gabureac, A. Ghosh, A. Fuhrer, S. F. Alvarado, and P. Gambardella, Interplay of spin-orbit torque and thermoelectric effects in ferromagnet/normal-metal bilayer, *Phys. Rev. B* **90**, 224427 (2014).
- 21) T. Nan, S. Emori, C. T. Boone, X. Wang, T. M. Oxholm, J. G. Jones, B. M. Howe, G. J. Brown, and N. X. Sun, Comparison of spin-orbit torques and spin pumping across NiFe/Pt and NiFe/Cu/Pt interfaces, *Phys. Rev. B* **91**, 214416 (2015).
- 22) K. Kondou, H. Sukegawa, S. Kasai, S. Mitani, Y. Niimi, and Y. Otani, Influence of inverse spin Hall effect in spin-torque ferromagnetic resonance measurements, *Appl. Phys. Express* **9**, 023002 (2016).
- 23) K. Ueda, M. Mann, P. W. P. de Brouwer, D. Bono, and G. S. D. Beach, Temperature dependence of spin-orbit torques across the magnetic compensation point in a ferrimagnetic TbCo alloy film, *Phys. Rev. B* **96**, 064410 (2017).
- 24) Y. Takeuchi, C. Zhang, A. Okada, H. Sato, S. Fukami, and H. Ohno, Spin-orbit torques in high-resistivity-W/CoFeB/MgO, *Appl. Phys. Lett.* **112**, 192408 (2018).
- 25) W.-B. Liao, C.-Y. Lin, T.-Y. Cheng, C.-C. Huang, T.-Y. Chen, and C.-F. Pai, Processing effect on spin-orbit torque switching and efficiency characterization in perpendicularly magnetized pillar devices, *Phys. Rev. Materials* **7**, 104409 (2023).
- 26) T. Nan, T. J. Anderson, J. Gibbons, K. Hwang, N. Campbell, H. Zhou, Y. Q. Dong, G. Y. Kim, D. F. Shao, T. R. Paudel, N. Reynolds, X. J. Wang, N. X. Sun, E. Y. Tsymbal, S. Y. Choi, M. S. Rzchowski, Yong Baek Kim, D. C. Ralph, and C. B. Eom, Anisotropic spin-orbit torque generation in epitaxial SrIrO₃ by symmetry design, *Proc. Natl. Acad. Sci.* **116**, 33 (2019).
- 27) A. S. Everhardt, D. C. Mahendra, X. Huang, S. Sayed, T. A. Gosavi, Y. Tang, C.-C. Lin, S. Manipatruni, I. A. Young, S. Datta, J.-P. Wang, and R. Ramesh, Tunable charge to spin conversion in strontium iridate thin films, *Phys. Rev. Mater.* **3**, 051201 (2019).
- 28) L. Liu, Q. Qin, W. Lin, C. Li, Q. Xie, S. He, X. Shu, C. Zhou, Z. Lim, J. Yu, W. Lu, M. Li, X. Yan, S. J. Pennycook, and J. Chen, Current-induced magnetization switching in all-oxide heterostructures, *Nat. Nanotechnol.* **14**, 939 (2019).
- 29) X. Huang, S. Sayed, J. Mittelstaedt, S. Susarla, S. Karimeddiny, L. Caretta, H. Zhang, V. A. Stoica, T. Gosavi, F. Mahfouzi, Q. Sun, P. Ercius, N. Kioussis, S. Salahuddin, D. C. Ralph,

- R. Ramesh, Novel Spin–Orbit Torque Generation at Room Temperature in an All-Oxide Epitaxial $\text{La}_{0.7}\text{Sr}_{0.3}\text{MnO}_3/\text{SrIrO}_3$ System, *Adv. Mater.* **33**, 2008269 (2021).
- 30) S. Hori, K. Ueda, T. Kida, M. Hagiwara, J. Matsuno, Spin–orbit torque generation in bilayers composed of CoFeB and epitaxial SrIrO_3 grown on an orthorhombic DyScO_3 substrate, *Appl. Phys. Lett.* **121**, 022402 (2022).
- 31) A. Bose, J. N. Nelson, X. S. Zhang, P. Jadaun, R. Jain, D. G. Schlom, D. C. Ralph, D. A. Muller, K. M. Shen, and R. A. Buhrman, Effects of Anisotropic Strain on Spin-Orbit Torque Produced by the Dirac Nodal Line Semimetal IrO_2 , *ACS Appl. Mater. Interfaces* **12**, 55411 (2020).
- 32) M. Patton, G. Gurung, D.-F. Shao, G. Noh, J. A. Mittelstaedt, M. Mazur, J.-. Kim, P. J. Ryan, E. Y. Tsymbal, S.-Y. Choi, D. C. Ralph, M. S. Rzchowski, T. Nan, and C.-B. Eom, Symmetry Control of Unconventional Spin–Orbit Torques in IrO_2 , *Adv. Mater.* **35**, 2301608 (2023).
- 33) K. Ueda, N. Moriuchi, K. Fukushima, T. Kida, M. Hagiwara, and J. Matsuno, Spin-orbit torque generation in NiFe/IrO_2 bilayers, *Phys. Rev. B* **102**, 134432 (2020).
- 34) K. Ueda, N. Moriuchi, K. Fukushima, T. Kida, M. Hagiwara, and J. Matsuno, Stacking-Order Effect on Spin-Orbit Torque, Spin Hall Magnetoresistance, and Magnetic Anisotropy in $\text{Ni}_{81}\text{Fe}_{19}\text{-IrO}_2$ Bilayers, *Phys. Rev. Appl.* **16**, 034039 (2021).
- 35) K. Ueda, H. Fujii, T. Kida, M. Hagiwara, J. Matsuno, Spin current generation from an epitaxial tungsten dioxide WO_2 , *APL Mater.* **11**, 061125 (2023).
- 36) H. Y. Hwang and S.-W. Cheong, Enhanced intergrain tunneling magnetoresistance in half-metallic CrO_2 films, *Science* **278**, 5343 (1997).
- 37) K. Suzuki and P. M. Tedrow, Resistivity and magnetotransport in CrO_2 films, *Phys. Rev. B* **58**, 17 (1998).
- 38) A. A. Bolzan, C. Fong, B. J. Kennedy, and C. J. Howard, Structural Studies of Rutile-Type Metal Dioxides, *Acta Crystallogr. B* **53**, 373 (1997).
- 39) L. Cao, X. Zhang, J. Yuan, L. Guo, T. Hong, W. Hang, and Y. Ma, Study on the Influence of Sapphire Crystal Orientation on Its Chemical Mechanical Polishing, *Appl. Sci.* **10**, 8065 (2020).
- 40) M. Uchida, W. Sano, K. S. Takahashi, T. Koretsune, Y. Kozuka, R. Arita, Y. Tokura, and M. Kawasaki, Field-direction control of the type of charge carriers in nonsymmorphic IrO_2 , *Phys. Rev. B* **91**, 241119(R) (2015).
- 41) M. Negishi, K. Fujiwara, and A. Tukazaki, Formation of ilmenite-type single-crystalline MgTiO_3 thin films by pulsed-laser deposition, *AIP Advances* **11**, 125125 (2021).
- 42) Y. Sun, Y. Zhang, C.-X. Liu, C. Felser, and B. Yan, Dirac nodal lines and induced spin Hall effect in metallic rutile oxides, *Phys. Rev. B* **95**, 235104 (2017).
- 43) Y. Ishikuro, M. Kawaguchi, N. Kato, Y.-C. Lau, and M. Hayashi, Dzyaloshinskii-Moriya

- interaction and spin-orbit torque at the Ir/Co interface, *Phys. Rev. B* **99**, 134421 (2019).
- 44) G. E. Bauer, E. Saitoh, and B. J. van Wees, Spin caloritronics, *Nat. Mater.* **11**, 391 (2012).
- 45) K. Uchida, S. Takahashi, K. Harii, J. Ieda, W. Koshibae, K. Ando, S. Maekawa, and E. Saitoh, Observation of the spin Seebeck effect, *Nature (London, UK)* **455**, 778 (2008).
- 46) A. V. Khvalkovskiy, V. Cros, D. Apalkov, V. Nikitin, M. Krounbi, K. A. Zvezdin, A. Anane, J. Grollier, and A. Fert, Matching domain-wall configuration and spin-orbit torques for efficient domain-wall motion, *Phys. Rev. B* **87**, 020402(R) (2013).
- 47) K. Fujiwara, Y. Fukuma, J. Matsuno, H. Idzuchi, Y. Niimi, Y. Otani, and H. Takagi, *5d* iridium oxide as a material for spin-current detection, *Nat. Commun.* **4**, 2893 (2013).
- 48) N. Nagaosa, J. Sinova, S. Onoda, A. H. MacDonald, and N. P. Ong, Anomalous Hall effect, *Rev. Mod. Phys.* **82**, 1539 (2010).
- 49) B. Zimmermann, K. Chadova, D. Ködderitzsch, S. Blügel, H. Ebert, D. V. Fedorov, N. H. Long, P. Mavropoulos, I. Mertig, Y. Mokrousov, and M. Gradhand, Skew scattering in dilute ferromagnetic alloys, *Phys. Rev. B* **90**, 220403(R) (2014).
- 50) S. Onoda, N. Sugimoto, and N. Nagaosa, Quantum transport theory of anomalous electric, thermoelectric, and thermal Hall effects in ferromagnets, *Phys. Rev. B* **77**, 165103 (2008).
- 51) E. Sagasta, Y. Omori, M. Isasa, M. Gradhand, L. E. Hueso, Y. Niimi, Y. Otani, and F. Casanova, Tuning the spin Hall effect of Pt from the moderately dirty to the superclean regime, *Phys. Rev. B* **94**, 060412(R) (2016).
- 52) M. Björck and G. Andersson, genx: An extensible X-ray reflectivity refinement program utilizing differential evolution, *J. Appl. Crystallogr.* **40**, 1174 (2007).
- 53) S. Lee, Y.-J. Lee, G. Lee, A. Soon, Activated chemical bonds in nanoporous and amorphous iridium oxides favor low overpotential for oxygen evolution reaction, *Nat. Commun.* **13**, 3171 (2022).
- 54) B. D. Cullity and S. R. Stock, *Elements of X-Ray Diffraction*, 3rd ed. (Prentice Hall, Upper Saddle River, NJ, 2001).

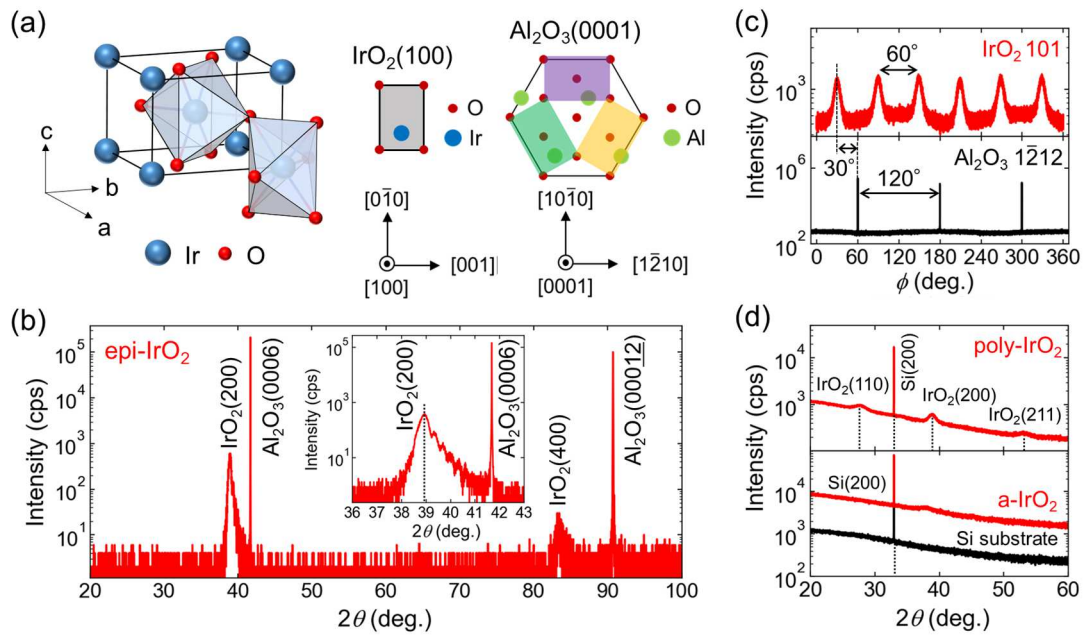


Fig. 1. (a) (left) Illustration of structure for rutile IrO₂. (right) The crystallographic relationship between the rutile-type IrO₂(100) and the Al₂O₃(0001). The purple, green, and yellow indicate three-type IrO₂ domains stemming from the trigonal symmetry of the Al₂O₃ substrate. (b) X-ray diffraction (XRD) 2θ-θ scan of epitaxial IrO₂ film grown on Al₂O₃(0001) substrate. Magnified view of the XRD scan around epitaxial IrO₂(200) reflection grown on the Al₂O₃(0001) substrate (Inset). (c) The azimuthal ϕ scan of (12̄12) diffraction for the Al₂O₃ substrate (bottom) and of (101) diffraction for IrO₂ film (top). (d) The XRD pattern of polycrystalline IrO₂ (top), and amorphous IrO₂ and thermally oxidized Si substrate (bottom).

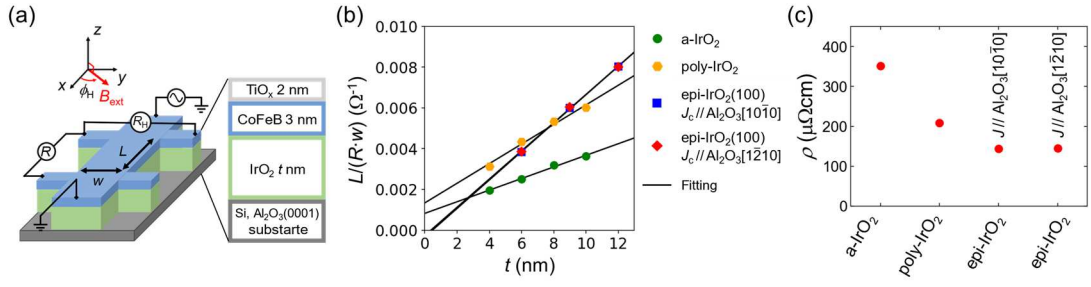


Fig. 2. (a) Schematic illustration of the device structure and layer geometry of the heterostructure samples. The ϕ_H represents the azimuthal angles of the external magnetic field (B_{ext}). AC current (J) is applied along the x axis direction. Hall resistance (R_H) and longitudinal resistance (R) are measured along y -axis and x -axis direction, respectively. (b) Sheet conductance as a function of the IrO_2 thickness (t) for amorphous, polycrystalline, and epitaxial IrO_2 with 3-nm-thick CoFeB layer. The solid lines show linear fitting on the data. (c) Electrical resistivity for amorphous, polycrystalline, and epitaxial IrO_2 . The direction of the J for epitaxial IrO_2 is along $[10\bar{1}0]$ and $[1\bar{2}10]$ orientations on the Al_2O_3 substrate.

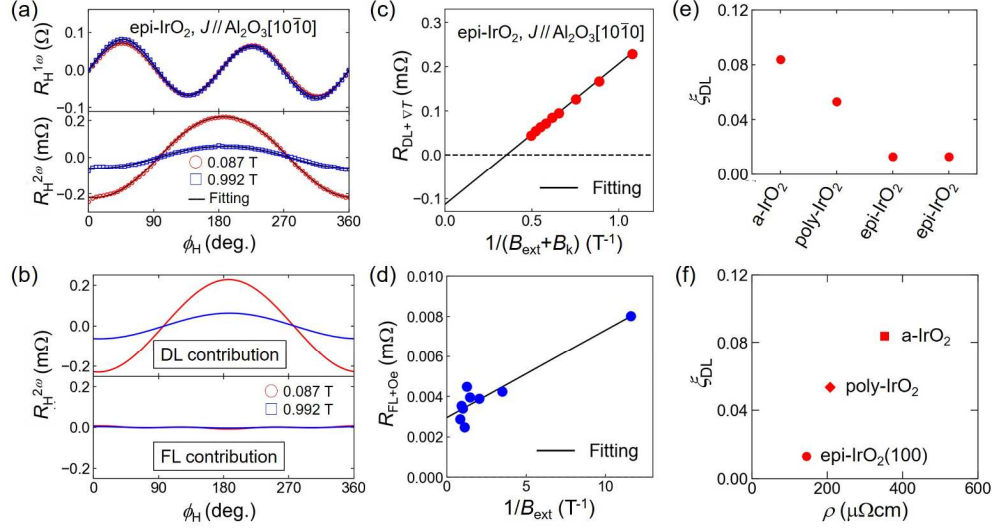


Fig. 3. (a) First-harmonic Hall resistance ($R_H^{1\omega}$) of 3-nm-thick CoFeB/6-nm-thick IrO₂ measured at 0.087 and 0.992 T with J along Al₂O₃(10 $\bar{1}$ 0) (top). The solid curve is fit to the data using Eq. (1). The corresponding second-harmonic Hall resistance ($R_H^{2\omega}$) with solid curve being fit using Eq. (2) (bottom). (b) DL contribution ($\cos\phi_H$) and FL contribution ($2\cos^3\phi_H - \cos\phi_H$) on the $R_H^{2\omega}$, separated from the fitting result. (c) The R_{DL+VT} as a function of $1/(B_{\text{ext}} + B_k)$ and (d) the R_{FL+Oe} as a function of $1/B_{\text{ext}}$. The solid line is linear fit to the experimental data. (e) DL SOT efficiency for amorphous, polycrystalline, and epitaxial IrO₂. The direction of the J for epitaxial IrO₂ is along [10 $\bar{1}$ 0] and [$\bar{1}$ 210] orientations of the Al₂O₃ substrate. (f) Relation of ζ_{DL} between ρ for epi-, poly-, and a-IrO₂.

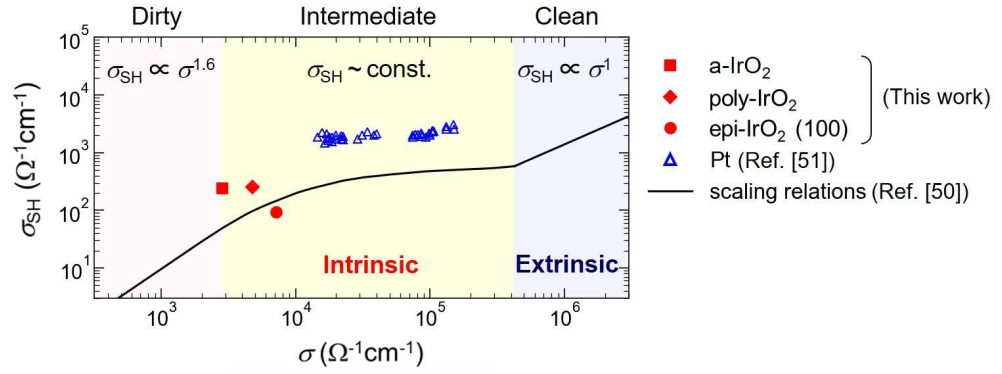


Fig. 4. The spin Hall effect scaling relation between spin Hall conductivity versus electrical conductivity in amorphous, polycrystalline, and epitaxial states of IrO₂, in comparison with polycrystalline Pt metal [51]. The black line represents the anomalous Hall effect scaling relation [50], which is dominated by the dirty, intermediate, and clean regimes.

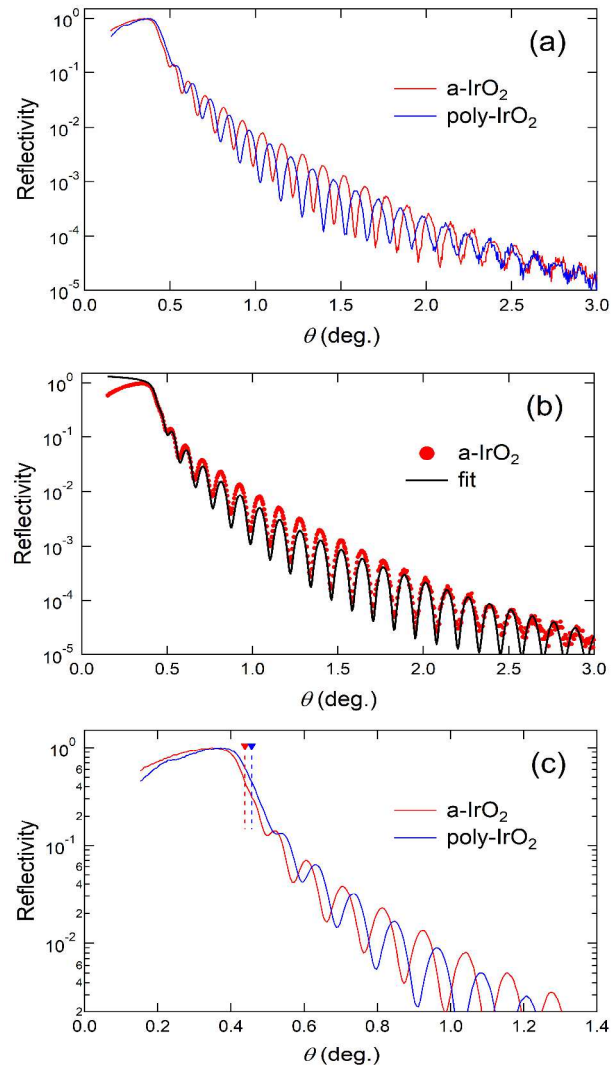


Fig. 5. (a) Wide-range x-ray reflectivity (XRR) profiles of IrO₂ films in amorphous (a-IrO₂) and polycrystalline (poly-IrO₂) states. (b) XRR profile of a-IrO₂ with the fitted curve. (c) Low-angle XRR profiles of amorphous and polycrystalline IrO₂, with critical angles indicated by red and blue triangles for a-IrO₂ and poly-IrO₂, respectively.

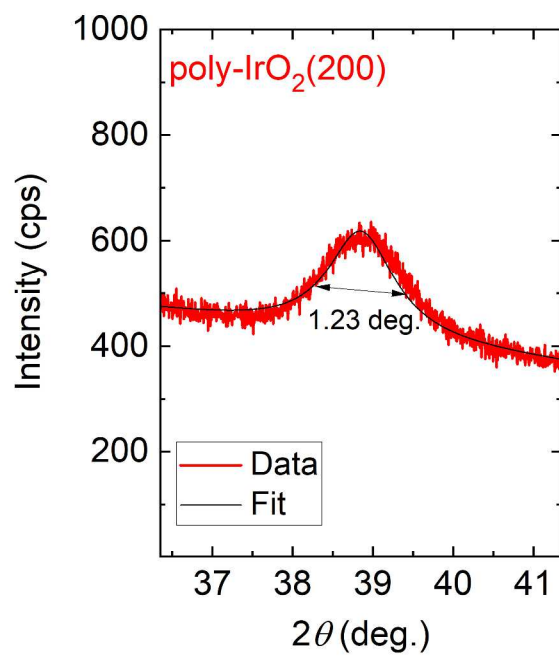


Fig. 6. Magnified view of x ray diffraction pattern for poly-IrO₂(200). Black solid curve represents a fit on data.